



Hidden symmetries generate rigid folding mechanisms in periodic origami

James McInerney^a, Bryan Gin-gé Chen^b, Louis Theran^c, Christian D. Santangelo^{d,e}, and D. Zeb Rocklin^{a,1}

^aSchool of Physics, Georgia Institute of Technology, Atlanta, GA 30332; ^bDepartment of Physics and Astronomy, University of Pennsylvania, Philadelphia, PA 19104; ^cSchool of Mathematics and Statistics, University of St. Andrews, St. Andrews KY16 9SS, Scotland; ^dDepartment of Physics, University of Massachusetts Amherst, Amherst, MA 01003; and ^eDepartment of Physics, Syracuse University, Syracuse, NY 13244

Edited by L. Mahadevan, Harvard University, Cambridge, MA, and accepted by Editorial Board Member John A. Rogers October 4, 2020 (received for review March 17, 2020)

We consider the zero-energy deformations of periodic origami sheets with generic crease patterns. Using a mapping from the linear folding motions of such sheets to force-bearing modes in conjunction with the Maxwell–Calladine index theorem we derive a relation between the number of linear folding motions and the number of rigid body modes that depends only on the average coordination number of the origami’s vertices. This supports the recent result by Tachi [T. Tachi, *Origami* 6, 97–108 (2015)] which shows periodic origami sheets with triangular faces exhibit two-dimensional spaces of rigidly foldable cylindrical configurations. We also find, through analytical calculation and numerical simulation, branching of this configuration space from the flat state due to geometric compatibility constraints that prohibit finite Gaussian curvature. The same counting argument leads to pairing of spatially varying modes at opposite wavenumber in triangulated origami, preventing topological polarization but permitting a family of zero-energy deformations in the bulk that may be used to reconfigure the origami sheet.

origami | mechanisms | rigid folding | topological polarization

Origami-inspired materials are thin sheets whose two-dimensional crease patterns control their three-dimensional mechanical response, now manufacturable at the macroscopic scale using shape-memory alloys (1, 2) and at the microscopic scale using graphene bilayers (3) or polymer films (4–6). Origami principles are used to engineer deployable solar cells (7), stent grafts (8), flexible electronics (9, 10), impact mitigation devices (11), and tunable antennas (12) as well as to characterize patterns in biological systems (13). Yet determining whether a crease pattern can be rigidly folded into a particular shape is a nondeterministic in polynomial-time-hard problem (14) due to nonlinear geometric constraints (15) that can lead to disjoint (16) or branched (17–20) configuration spaces with multiple energetic minima (21, 22).

Periodic origami sheets yield uniform mechanical properties such as negative Poisson ratios (23–27) and high stiffness-to-weight ratios (28), making them apt for the design of mechanical metamaterials. However, the study of origami tessellations has typically focused on crease patterns with inherent symmetries, such as the parallelogram faces of the Miura-ori (23, 24), which both simplify their analysis and generate rigid folding motions (29–31) that would cost energy in the absence of these symmetries (32). One might naively expect such symmetries are required as triangulations of all convex polyhedra are rigid (33). However, Tachi (34) recently found origami sheets composed of repeating unit cells with triangular but otherwise generic faces rigidly fold between cylindrical configurations, indicating that crease topology (the number of edges and vertices) may play as important a role as crease geometry (the angles between these edges) in determining origami kinematics.

In the present work, we similarly consider generic triangulations, which inform the general case in three vital ways. First, the rigidly foldable configurations of any origami sheet can be derived as a subset of its triangulation’s configurations. Sec-

ond, the low-energy deformations of origami sheets are often well approximated by the rigid configurations of their triangulations (35, 36). Finally, the triangulations are at the “Maxwell point”: They have an equal number of constraints and degrees of freedom (37, 38), which we emphasize by calling them Maxwell origami. Mechanical systems at the Maxwell point generically possess large numbers of both zero-energy modes and force-bearing modes (39, 40) which can be localized to the boundary via topological polarization (37, 38, 41), provide directional response in the bulk (42, 43), and be tuned by reconfigurations of the network (44). However, origami sheets possess a geometrical duality between these two classes of modes (33, 45, 46) that, as we show, both permits the rigid foldability (34) and modifies its topological class, prohibiting the topological polarization (47) of Maxwell origami which limits the ability to engineer directional response.

The remainder of this paper is organized as follows. First, we review the work of Tachi (34) to show Maxwell origami generically approximates a cylindrical sheet with two degrees of freedom. Next, we construct an index theorem that pairs folding motions with continuous symmetries in Maxwell origami. We then show the restriction to cylindrical configurations leads to distinct branches of nonlinearly foldable origami configurations that we confirm through numerical simulation. Finally, we extend our index theorem to accommodate spatially varying modes to explain the observed lack of topological polarization in

Significance

The traditional approach to designing origami metamaterials uses particular, highly symmetric crease patterns to generate folding motions for reconfigurability. We instead consider origami sheets with periodic but otherwise generic, asymmetric triangular faces and show they exhibit nonlinear folding motions which transform sheets through two-dimensional families of cylindrical configurations, with the addition of quadrilateral faces restricting sheets to one-dimensional subsets of configurations. This leads to a topological class of mechanical modes, preventing origami from exhibiting exponentially localized floppy modes observed in other systems. These results do not depend on scale or material and hence have applications extending to architecture and robotics, but particularly to the nanoscale, where limited control over fold patterns can constrain traditional techniques.

Author contributions: J.M., B.G.-g.C., L.T., C.D.S., and D.Z.R. designed research; J.M., B.G.-g.C., L.T., C.D.S., and D.Z.R. performed research; and J.M. wrote the paper.

The authors declare no competing interest.

This article is a PNAS Direct Submission. L.M. is a guest editor invited by the Editorial Board.

Published under the [PNAS license](#).

¹To whom correspondence may be addressed. Email: zebroclin@gatech.edu.

This article contains supporting information online at <https://www.pnas.org/lookup/suppl/doi:10.1073/pnas.2005089117/-DCSupplemental>.

First published November 16, 2020.

Maxwell origami (47) and report lines of bulk modes with real wavenumber.

$$\mathbf{S}_{1(2)} \equiv \prod_{1(2)} \mathbf{R}(\rho_{(i,j)}, \hat{\mathbf{r}}_{(i,j)}) \quad [2]$$

Cylindrical Symmetries as a Consequence of Periodic Origami Angles

Origami sheets are parameterized by fixed patterns of straight creases along which they can be folded rigidly, in the sense that no face bends or stretches. This rigidity constraint determines what folded configurations are compatible with the underlying crease pattern. Here, we introduce our notation and describe the most general origami structures with periodic folds, as previously explored by Tachi (34).

We consider origami composed of unit cells, as depicted in Fig. 1A, with sector angles $\alpha_{(i,j,k)}$ subtended by vertex-sharing edges $\mathbf{r}_{(i,j)}$ and $\mathbf{r}_{(i,k)}$, and fold angles $\rho_{(i,j)}$, given by the supplement of the respective dihedral angles, between pairs of adjacent faces (defined such that $\rho_{(i,j)} = 0$ in a flat sheet), are identical in every cell, which are themselves indexed by $\mathbf{n} = (n_1, n_2)$. We do not require that the origami be developable, so that the sector angles need not sum to 2π around a vertex.

A necessary and sufficient condition for a set of fold angles to compose a valid rigid fold about a vertex is for the successive rotations induced by traveling about the vertex to yield the identity rotation. This leads to the vertex condition derived in *SI Appendix, section 1* (15),

$$\mathbf{F}_i = \prod_{(i,j)} \mathbf{R}_z(\alpha_{(i,j,k)}) \mathbf{R}_x(\rho_{(i,j)}) = \mathbf{I}, \quad [1]$$

where j, k takes on the successive indexes of vertices connected to vertex i in counterclockwise order and $\mathbf{R}_x, \mathbf{R}_z$ are matrices representing rotations about the x and z axes. For a simply connected sheet (as opposed to kirigami sheets with holes), this condition imposed at each vertex is sufficient to ensure rigid folding of the entire sheet.

Furthermore, the periodicity of sector angles between cells ensures that periodic fold angles can satisfy this condition in every cell. However, such periodic angles do not ensure that adjacent cells will have the identical orientations of normal crystalline structures. Instead, lattice rotation matrices

will relate the orientations between two faces in adjacent cells, where the products are taken over edges on paths between the two faces. This also means that the lattice vectors obtained by summing along edges, $\mathbf{I}_{1(2)} \equiv \sum_{1(2)} \mathbf{r}_{(i,j)}$, can only be defined in the first cell and undergo rotations given by the lattice rotation matrices in other cells. Hence, in contrast with a conventional crystal whose cells are translations of one another along lattice vectors, the origami sheet is screw periodic: Cells are related by screw motions consisting of translations and rotations (Fig. 1B).

Any valid configuration, satisfying Eq. 1, must define unique relative orientations and positions of cells regardless of the path between them. Considering a loop between cells, such as the four colored cells in Fig. 1B, leads to the intercell position and compatibility conditions,

$$\mathbf{S}_1 \mathbf{S}_2 = \mathbf{S}_2 \mathbf{S}_1, \quad [3]$$

$$\mathbf{I}_1 + \mathbf{S}_1 \mathbf{I}_2 = \mathbf{I}_2 + \mathbf{S}_2 \mathbf{I}_1. \quad [4]$$

These conditions imply there is a unique rotation axis (except for flat sheets and a few pathological cases that we do not consider), denoted by $\hat{\mathbf{s}}$, and a unique radius of curvature so that the sheet generically approximates a cylinder as shown in Fig 1B (see *SI Appendix, section 2* for a characterization of this cylinder) (34). The familiar case of spatially periodic origami then emerges as the special limit in which the lattice rotations, $\mathbf{S}_{1,2}$, become identity matrices while arbitrary configurations with nonzero Gaussian curvature cannot be rigidly folded from periodic angles. Given the position of each vertex in the origin cell, denoted by \mathbf{r}_i , we can compute the position of an arbitrary vertex by summation of all edge vectors traveled along to reach it,

$$\mathbf{r}_i(\mathbf{n}) = \sum_{n'=0}^{n_1-1} \mathbf{S}_1^{n'} \mathbf{I}_1 + \mathbf{S}_1^{n_2} \sum_{n''=0}^{n_1-1} \mathbf{S}_2^{n''} \mathbf{I}_2 + \mathbf{S}_1^{n_1} \mathbf{S}_2^{n_2} \mathbf{r}_i, \quad [5]$$

where the order of summation can be interchanged by orientation and position compatibility (Eqs. 3 and 4) (see *SI Appendix, section 3* for an evaluation of the summations over lattice rotations).

Those compatibility conditions allow a prediction for the dimension of the space of cylindrical configurations of a triangulated origami. Consider a potential configuration specified by the positions of each vertex, the two lattice vectors, and the two lattice rotation matrices. A rigidly folded configuration of the triangulation must preserve the length of each edge and satisfy position and orientation compatibility. Euler's polyhedron formula states that the numbers of faces, edges, and vertices must satisfy $N_v - N_e + N_f = \chi$, where the Euler characteristic χ vanishes for a doubly periodic surface. Every face in a triangulation has three edges, each shared with exactly one face so that $N_e = (3/2)N_f$, thereby implying $N_e = 3N_v$. In this way, each three-dimensional vertex position is accounted for via three edge constraints. Additionally, there are 12 numbers that specify the lattice vectors and lattice rotation matrices. The compatibility conditions supply four constraints: that the direction of the axis of the second rotation is shared by that of the first and that two components of the position vectors in Eq. 4 are equal (the third direction, along the shared axis, is guaranteed to be equal). This leaves an eight-dimensional space of configurations of the sheet, six of which are simply rigid rotations and translations, leaving a two-dimensional space of rigidly foldable deformations. This was observed by Tachi (34), who advanced a similar counting argument. We will see these deformations emerge explicitly by considering higher-order rigidity conditions, which also reveal subtle branching behavior around the flat state.

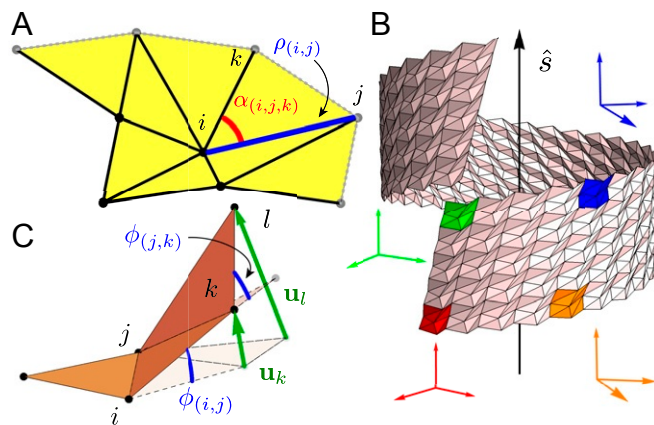


Fig. 1. (A) An origami unit cell with vertices labeled by Roman indexes, sector angles labeled by $\alpha_{(i,j,k)}$, and fold angles labeled by $\rho_{(i,j)}$. (B) A generic, periodic origami sheet with cylindrical symmetries that follow from vertex compatibility with the unit cell highlighted in yellow. The screw periodicity of these sheets implies an orthonormal frame rotates between cells by the cell rotation matrices $\mathbf{S}_{1(2)}$. (C) The zero modes of an origami sheet can be specified either by the vertex displacements, \mathbf{u}_i , on every vertex i or the changes in folding angles, $\phi_{(i,j)}$, on every edge (i, j) . The vertex displacements due to a folding motion accumulate, allowing for nonzero curvature.

Helical, cylindrical tubes have the two additional constraints that the ratios of lattice rotation angles, $2\pi\theta_1/\theta_2$, and on-axis components of the lattice vectors l_1^s/l_2^s are rational to ensure closure, which generically renders the tubes rigid. Allowing the tube to close without vertices connecting relieves the second of these conditions and permits motion by slip with a single degree of freedom (48).

Linear Folding Motions from Global Symmetries via Vertex Duality

Relationship between Folding Angles and Vertex Displacements. The cylindrical symmetries of origami correspond to rigid body modes which are paired with force-bearing modes at the Maxwell point (49, 50). These force-bearing modes, however, are identical to infinitesimal changes in the fold angles, ϕ_{ij} , which satisfy the vertex condition, Eq. 1, to first order (33, 45, 46). Here, we combine this mechanical duality with the mechanical criticality of Maxwell origami to show rigid body modes generate linear folding motions independent of the sector angles.

Consider infinitesimal changes (zero modes) $\phi_{(i,j)}$ to the fold angles $\rho_{(i,j)}$. The linearization of Eq. 1, as shown in ref. 51 and recapitulated in *SI Appendix, section 4*, is

$$\sum_{(i,j)} \phi_{(i,j)}(\mathbf{n}) \hat{r}_{(i,j)}(\mathbf{n}) = \mathbf{0}, \quad [6]$$

where the edges rotate $\hat{r}_{(i,j)}(\mathbf{n}) = \mathbf{S}_1^{n_1} \mathbf{S}_2^{n_2} \hat{r}_{(i,j)}$ between cells by Eq. 5. The infinitesimal rotation of a face (i, j, k) may be described by an “angular velocity” vector $\omega_{(i,j,k)}$ such that any vector \mathbf{v} on the face, including edge vectors, undergoes a rotation $\mathbf{v} \rightarrow \mathbf{v} + \omega_{(i,j,k)} \times \mathbf{v}$ as shown in Fig. 1C. Two faces sharing an edge must then induce the same rotation upon it, leading to a relation between adjacent angular velocities and the folding angle of the edge between them:

$$\omega_{(i,j,l)} - \omega_{(i,j,k)} = \phi_{(i,j)} \hat{r}_{(i,j)}. \quad [7]$$

These then accumulate such that the angular velocity of one face relative to a fixed face is

$$\omega_{(i,j,k)}(\mathbf{n}) = \sum_{(i',j')} \phi_{(i',j')}(\mathbf{n}') \hat{r}_{(i',j')}(\mathbf{n}'), \quad [8]$$

where the sum is over all edges crossed on a path between the faces. Similarly, the displacement of a vertex on a distant face is given by the sum of all vertex displacements along the path from a fixed vertex, which are in turn determined by rotating the bond vectors via their respective angular velocities:

$$\mathbf{u}_k(\mathbf{n}) = \sum_{(i',j')} \omega_{(i',j',k')}(\mathbf{n}') \times \mathbf{r}_{(i',j')}(\mathbf{n}'). \quad [9]$$

This summation is explicitly evaluated for both the spatially periodic and screw periodic cases in *SI Appendix, section 7*.

Having described how vertex positions may be generated via arbitrary folding motions, we may complete the identification by a map from the vertex positions of an isometry back to the folding motions. The procedure is to take two edge vectors along a face, $\mathbf{r}_{(i,j)}$, $\mathbf{r}_{(k,j)}$, and the normal vector $\mathbf{N}_{(i,j,k)} = \mathbf{r}_{(i,j)} \times \mathbf{r}_{(k,j)}$ and to consider the changes implied by the vertex displacements to the two vectors $\mathbf{u}_{(i,j)}$, $\mathbf{u}_{(k,j)}$ and to the normal vector $\delta\mathbf{N}_{(i,j,k)} = \mathbf{r}_{(i,j)} \times \mathbf{u}_{(k,j)} + \mathbf{u}_{(i,j)} \times \mathbf{r}_{(k,j)}$. This yields the matrix equation

$$\omega_{(i,j,k)}^\times(\mathbf{r}_{(i,j)} \quad \mathbf{r}_{(k,j)} \quad \mathbf{N}_{(i,j,k)}) = (\mathbf{u}_{(i,j)} \quad \mathbf{u}_{(k,j)} \quad \delta\mathbf{N}_{(i,j,k)}) \quad [10]$$

which may be inverted to obtain $\omega_{(i,j,k)}^\times$, the cross-product matrix whose elements give the angular velocity of the face. From these angular velocities Eq. 7 may be used to obtain the changes to the folding angles.

Duality between Folding Motions and Tensions. The linear folding constraint, Eq. 6, takes the familiar form of tensions $t_{(i,j)}$ along edges $\hat{r}_{(i,j)}$ that yield no net force called states of self-stress (33, 45, 46). This hidden symmetry between static and kinematic modes has particular significance for periodic sheets, for which it implies symmetrically distributed edge modes, as we discuss later. The concatenation of Eq. 6 at each vertex within the origin cell yields the equilibrium matrix, \mathbf{Q} , that maps tensions to the net force on each vertex. Importantly, the static–kinematic duality reveals that the transpose of the equilibrium matrix is the compatibility matrix, $\mathbf{C} = \mathbf{Q}^T$, that maps vertex displacements to bond extensions (50). This leads, via the rank-nullity theorem of linear algebra, to the celebrated Maxwell–Calladine index theorem relating the number of zero-energy vertex displacements, N_{zm} , to the number of states of self-stress, N_{ss} , within the origin cell (49, 50)

$$N_{zm} - N_{ss} = 3N_v - N_e. \quad [11]$$

We are now able to combine the criticality of triangulated origami, which ensures the right-hand side vanishes, with the duality between states of self-stress and folding modes to use spatial symmetries to guarantee the existence of folding modes, some of which have already been observed. Spatially periodic sheets have three translational modes, implying three states of self-stress and three folding motions, as observed in triangulations of the Miura-ori and eggbox crease patterns (23–27). In contrast, cylindrical sheets have only two rigid-body modes: translations along and rotations about the axis, implying the two linear motions lead to a two-dimensional space of configurations. In either case, fusing two triangular faces together to create a quadrilateral face eliminates a degree of freedom, reducing the space of rigid configurations. More generally, folding motions are possible in origami above the Maxwell point due to symmetries, e.g., the Miura-ori, that render constraints degenerate as has been observed in spring networks (52).

Nonlinear Constraints Lead to Branching between Cylindrical Configurations

In this section, we describe the full set of nonlinear rigid folds of the origami sheets. Spatially periodic states have three linear modes and we employ second-order rigidity conditions to identify how they extend to the nonlinear branches. As we show, the necessary requirement that the linear modes generate a cylindrical surface is sufficient for a second-order folding motion to exist. The surface of modes in configuration space (parameterized by the fold angles) is generally two-dimensional, with two two-dimensional branches connected at the flat state. In contrast, in developable sheets up to 2^{N_v+1} branches can meet at the flattened state, with every sheet investigated showing pairs of branches distinguished by whether a vertex pops upward or downward, as previously observed in origami sheets with one-dimensional configuration spaces (19).

While first-order compatibility is sufficient to ensure a cylindrical configuration folds into another cylindrical configuration (*SI Appendix, section 7*), the lattice rotation axes spontaneously chosen when folding from a spatially periodic state are not necessarily coaxial. We can see this by noting the expansion of orientation compatibility, Eq. 3, about the flat state, where the lattice rotations are identity matrices, is trivially satisfied to first order. Instead, the leading-order contribution is given by

$$\delta\mathbf{S}_1 \delta\mathbf{S}_2 = \delta\mathbf{S}_2 \delta\mathbf{S}_1, \quad [12]$$

where the $\delta\mathbf{S}_{1,2}$ are skew-symmetric generators of rotation whose components are given by the intercell angular velocity $\sum_{1,2} \phi_{(i,j)} \hat{r}_{(i,j)}$ computed from Eq. 8 (*SI Appendix, section 7*). From position compatibility, Eq. 4, we have at first order $\delta\mathbf{S}_1 \mathbf{l}_2 = \delta\mathbf{S}_2 \mathbf{l}_1$, implying these rotations lie in the plane of the

origami sheet defined by $\mathbf{l}_1 \times \mathbf{l}_2$ so that Eq. 12 has only a single nonzero entry. Taking linear combinations of the linear folding motions, $\phi_{(i,j)} = \sum_{\alpha} \lambda_{\alpha} \phi_{(i,j)}^{\alpha}$, this becomes a quadratic expression in the real coefficients, λ_{α} , which will generically admit two distinct families of solutions, λ_{α}^{\pm} , that correspond to upward- or downward-folded cylinders. We note real solutions to Eq. 12 do not always exist, as is the case for the triangulated Miura-ori, which prevents its out-of-plane linear motions from extending nonlinearly (23); however, we find real solutions generically exist for our Maxwell origami sheets without any fine tuning.

That the linear folding motions yield a cylindrical configuration turns out to be a sufficient condition for the existence of second-order folding motions, $\delta\phi_{(i,j)}$, which satisfy the vertex constraint, Eq. 1, to second order. This second-order vertex condition consists of a linear term in $\delta\phi_{(i,j)} \hat{\mathbf{r}}_{(i,j)}$ and a quadratic sum of pairwise products of $\phi_{(i,j)} \hat{\mathbf{r}}_{(i,j)}$ over each edge connected to a particular vertex i (see *SI Appendix, section 5* for an expansion of Eq. 1),

$$\sum_{(i,j)} \delta\phi_{(i,j)} \hat{\mathbf{r}}_{(i,j)} + \sum_{(i,j)} \phi_{(i,j)} \left(\sum_{\substack{(i,k) \\ k < j}} \phi_{(i,k)} \hat{\mathbf{r}}_{(i,k)} \right) \times \hat{\mathbf{r}}_{(i,j)} = \mathbf{0}, \quad [13]$$

where $k < j$ denotes the interior sum is taken over successive indexes clockwise from j up to the starting edge. The interior sum of the second term gives, by Eq. 8, the angular velocity of a face relative to the starting face at vertex i so that the cross product gives the rotation of edge $\hat{\mathbf{r}}_{(i,j)}$ with the first edge of the sum held fixed. By the first-order condition, Eq. 6, we can add any constant angular velocity, ω_i , to this sum since the exterior sum $\omega_i \sum \phi_{(i,j)} \times \hat{\mathbf{r}}_{(i,j)}$ vanishes, allowing us to rewrite Eq. 13 as

$$\sum_{(i,j)} \delta\phi_{(i,j)} \hat{\mathbf{r}}_{(i,j)} + \sum_{(i,j)} \phi_{(i,j)} \delta\hat{\mathbf{r}}_{(i,j)} = \mathbf{0}, \quad [14]$$

where $\delta\hat{\mathbf{r}}_{(i,j)}$ depends on the coefficients, λ_{α} , used to construct the linear folding motion which are themselves linear in the $\phi_{(i,j)}$. This means when we concatenate Eq. 14 at each vertex, the first term is the action of the equilibrium matrix on the second-order folding motions, $\mathbf{Q}\delta\phi$, while the second term is the action of the change in the equilibrium matrix due to a linear folding motion on the linear folding motions, $\delta\mathbf{Q}\phi$, where we use boldface type to denote the vector of fold angle changes $\phi = (\dots, \phi_{(i,j)}, \dots)$.

Since we have already restricted our linear folding motions to those which yield cylindrical configurations, the compatibility matrix of the linearly deformed state, $\mathbf{C}' = \mathbf{C} + \delta\mathbf{C}$, must admit zero modes, \mathbf{u}' , corresponding to translations and rotations about the uniquely defined axis. These are paired with states of self-stress, \mathbf{t}' , that lie in the nullspace of the new equilibrium matrix, $\mathbf{Q}' = \mathbf{Q} + \delta\mathbf{Q}$, via mechanical criticality which, by the mechanical duality, are isomorphic to linear folding motions ϕ' . Such new linear folding motions can generically be written as a combination of the linear folding motions in the original configuration, ϕ , along with a correction, $\delta\phi$, that satisfies Eq. 14 after dropping the higher-order term $\delta\mathbf{Q}\delta\phi$. Hence, the existence of the second-order folding motions of Eq. 14 is guaranteed as long as the first-order motions generate a cylindrical surface. As shown explicitly in *SI Appendix, section 6*, this result can also be derived via the mechanical duality, which reveals a connection between rigid translations and rotations.

Finally, let us consider developable origami sheets in the flat state which admit extra linear folding motions (the generalization to origami sheets with both developable and nondevelopable vertices is straightforward). This can be seen by noting Eq. 6 furnishes only two constraints per vertex when all edges lie in

a plane. These additional folding motions are paired with zero modes that correspond to vertices popping up or down out of the plane (19, 20). Generally, this yields an extra $N_v - 1$ linear folding motions for developable origami in the flat state (the rigid-body translation in the direction normal to the sheet can be written as a linear combination of the N_v additional modes arising from developability) which do not all extend to rigid folding motions. The N_v seemingly missing constraints are provided by the quadratic term in Eq. 13. Since every edge lies in the same plane, this yields a single constraint per vertex. Moreover, this term is in the left nullspace of the equilibrium matrix so no $\delta\phi_{(i,j)}$ are needed to satisfy Eq. 1 to second order. We generalize our definition of sector angles so that $\alpha_{(i,j,k)}$ is the angle between edges $\mathbf{r}_{(i,j)}$ and $\mathbf{r}_{(i,k)}$ which do not necessarily share a face but are coplanar. Eq. 13 then simplifies to the scalar equation for a developable vertex i :

$$\sum_{(i,j)} \sum_{\substack{(i,k) \\ k > j}} \phi_{(i,j)} \phi_{(i,k)} \sin(\alpha_{(i,j,k)}) = 0. \quad [15]$$

By taking linear combinations of our folding motions, we can find simultaneous solutions to the N_v second-order constraints. While there are up to 2^{N_v+1} complex roots by Bézout's theorem (19, 53), we are interested only in the real-valued solutions whose existence depends on the crease geometry. Since a developable sheet has reflection symmetry through the plane of the sheet, these roots come in pairs which fold upward or downward into indistinguishable cylinders. In other words, for N branches there are only $N/2$ unique branches which cannot be obtained by rotations of the remaining $N/2$ branches.

Numerical Investigation of Nonlinear Folding

We now show corrections exist at all orders by numerically evolving periodic origami sheets. We begin with a spatially periodic, nondevelopable origami sheet composed of six triangular faces and a single quadrilateral face in each cell (this unit cell with four vertices is the simplest pattern with no trivial creases), as labeled by the star in Fig. 2, which rigidly fold along its one-dimensional branches. Following, we add a crease across the diagonal of the quadrilateral face, allowing the sheet to explore its two-dimensional space of rigidly foldable configurations embedded in the N_e -dimensional configuration space. Alternatively we may obtain a one-dimensional path through the two-dimensional configuration space by locking the fold angle on any edge whether or not the adjacent faces form a polygon. To visualize this surface, we project into a three-dimensional space spanned by strains of the lattice vectors. We use the three independent components, $(\epsilon_{11}, \epsilon_{22}, \epsilon_{12})$, of the in-plane deformation tensor determined via changes to the lengths and angle between the lattice vectors as described in *SI Appendix, section 9*.

In Fig. 2, we show the branched one-dimensional paths and the two-dimensional surfaces corresponding to configurations of the origami sheet along with a spatial configuration of the sheet on each branch (see *Movie S1* for evolution along this surface). The branches are colored according to the configuration's radius of curvature at each state, where the sign is chosen to designate whether the sheet folded upward or downward. In *SI Appendix, section 8*, we discuss how the spatial embedding and curvature direction of these configurations is obtained from the fold angles. These trajectories close when allowing for self-intersection of the origami sheet (some fold angles pass through $\pm\pi$ at which point adjacent faces intersect), as shown in Fig. 2, *Inset* which, although unphysical for origami, may have consequences in the behavior of equivalent systems such as spin origami (54). Although the two-dimensional surfaces close, we show only a closed one-dimensional path as otherwise features are obscured by spurious self-intersections due to different

configurations with the same in-plane strains despite having distinct fold angles.

We next construct a developable origami sheet with a single quadrilateral face in the flat state. Our arbitrarily chosen crease pattern yields six real solutions to Eq. 15, indicating six branches from the flat state. We show three of these branches in Fig. 3 (each branch has a beginning and an end which join in the flat state), all with positive radius of curvature (see *Movie S2* for evolution along this surface). The remaining three branches have the exact same in-plane strains with equal and opposite radii of curvature. The number of branches is a property of the crease geometry and we do not address a method for controlling the number of branches here. In fact, even identical triangulations with different faces fused into a quadrilateral substantially affect which strains and curvatures (geometry) occur in addition to the number of branches (topology). For developable origami, the lattice vectors are maximal in the flattened state so any folding results in $\epsilon_{11}, \epsilon_{22} < 0$, while shearing allows for either positive or negative values of ϵ_{12} .

Pairing of Spatially Varying Modes at Opposite Wavenumbers

In the previous sections we considered the pairing of rigid-body modes and deformations with the same fold angle changes in every cell. Here, we generalize the mechanical duality to spatially varying modes to investigate the topological mechanics of Maxwell origami whose connections to quantum mechanical sys-

tems such as topological insulators (41), nodal semimetals (42), dissipative systems (55), and spin origami (54, 56–58) are discussed in *SI Appendix, section 10*. These spatially varying zero modes are normal modes of the system (with frequency zero) and so, due to Bloch's theorem, must take the forms

$$\mathbf{u}_i(\mathbf{n}) = \mathbf{u}_i z_1^{n_1} z_2^{n_2}, \quad \phi_{(i,j)}(\mathbf{n}) = \phi_{(i,j)} z_1^{n_1} z_2^{n_2}, \quad [16]$$

for Bloch factors $z_i = e^{iq_i}$ with wavenumbers q_i which may be complex for general boundary conditions. The mapping from vertex displacements to folding motions in Eq. 9 extends naturally to the spatially varying modes, which inherit the same dependence on wavenumber so that, by the mechanical duality of origami, there is a mapping between zero modes and states of self-stress at finite wavenumber $N_{zm}(\mathbf{q}) = N_{ss}(\mathbf{q})$.

The finite wavenumber static-kinematic duality relates the equilibrium matrix to the transpose of the compatibility matrix at the opposite wavenumber, $\mathbf{Q}(\mathbf{q}) = \mathbf{C}^T(-\mathbf{q})$, modifying the Maxwell–Calladine index theorem of Eq. 11 to (37, 38)

$$N_{zm}(\mathbf{q}) - N_{ss}(-\mathbf{q}) = 3N_v - N_e, \quad [17]$$

which pairs zero modes at \mathbf{q} with self-stresses at $-\mathbf{q}$ (this sign difference, crucial for our argument, has been omitted previously). This leads to the intriguing scenario, identified by Kane and Lubensky (41), in which a zero mode may be exponentially localized to one edge (at some complex \mathbf{q}) with a state of self-stress at the opposite edge (at $-\mathbf{q}$), creating an excess or deficit

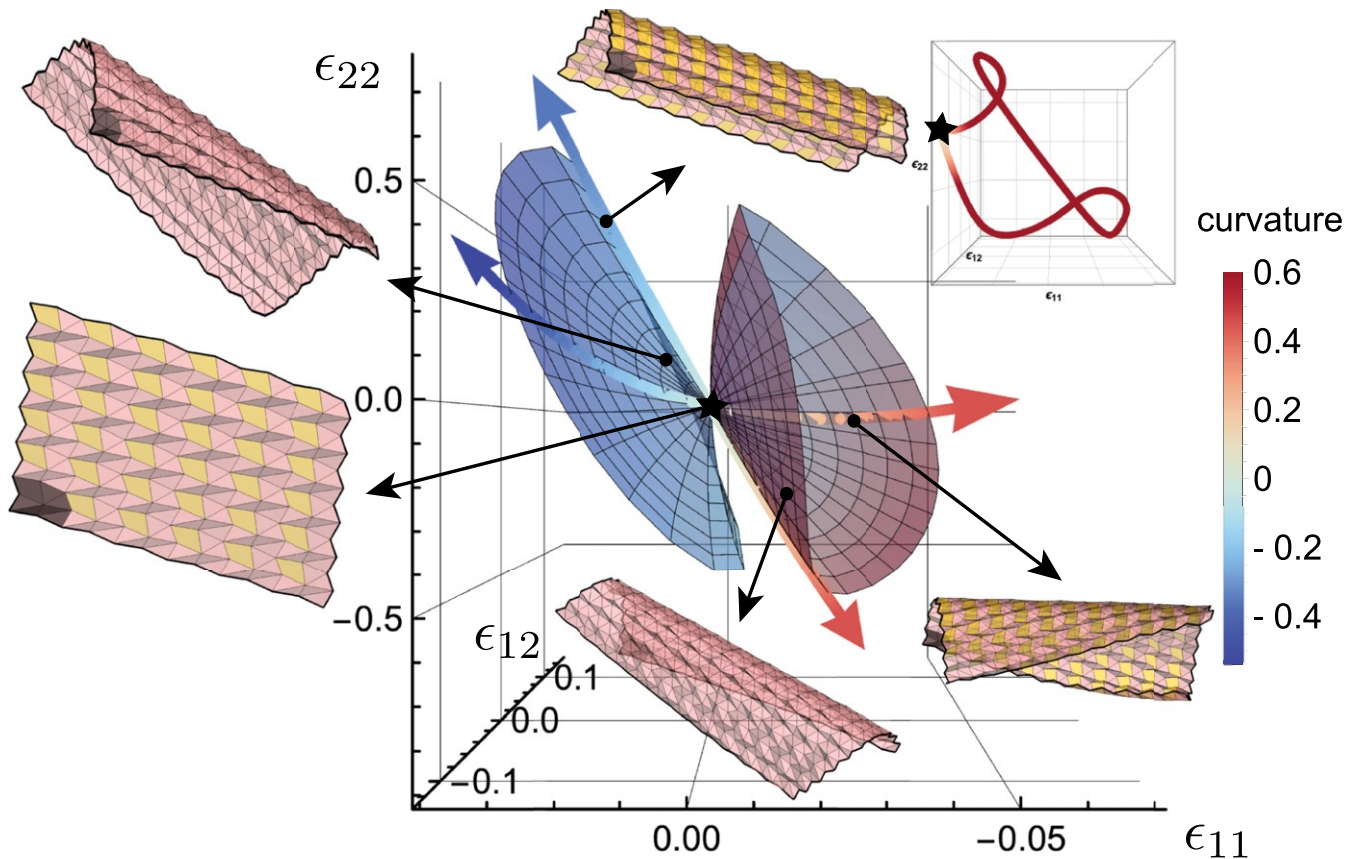


Fig. 2. The two-dimensional surface of rigidly foldable configurations for a nondevelopable triangulated origami sheet projected from its N_e -dimensional configuration space to the three-dimensional strain space (*SI Appendix, sections 8 and 9*), where coloring indicates the signed radius of curvature at each point. Arrows point from a point in this space to the corresponding reconstructed sheet with cell $\mathbf{n} = (0, 0)$ colored in gray. Some origami sheets have two triangular faces fused into a rigid quadrilateral marked in yellow, restricting the folding motions from the full 2D surfaces to one-dimensional paths marked with curved, multicolored arrows. The yellow quadrilateral indicates a polygonal face which restricts the sheet to one-dimensional trajectories. The distinct branches correspond to origami sheets which fold upward or downward from the flat state. Boxed *Inset* shows two one-dimensional folding trajectories as they close into a single loop over high strains.

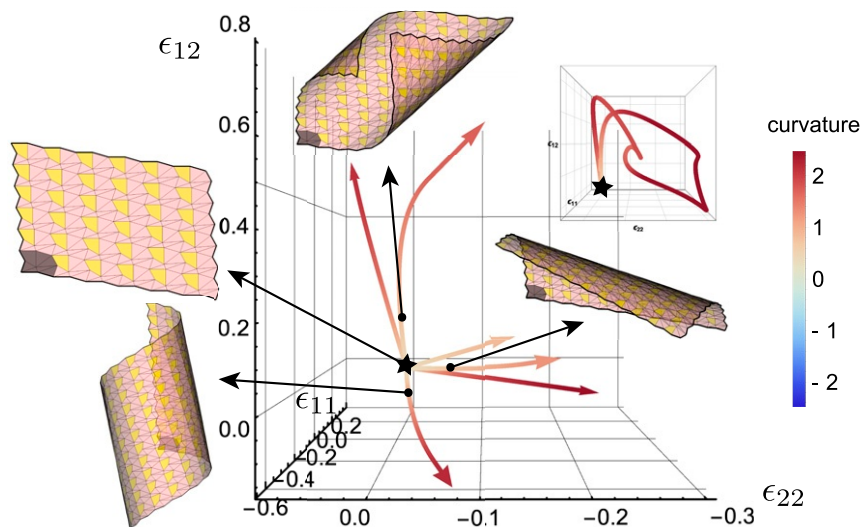


Fig. 3. The one-dimensional lines of rigidly foldable configurations for a developable origami sheet with one quadrilateral face per unit cell projected from its N_c -dimensional configuration space to the three-dimensional strain space (*SI Appendix, sections 8 and 9*), where coloring indicates the signed radius of curvature at each point where the flattened configuration is labeled by a star. Arrows point from a branch in this space to the corresponding reconstructed sheet with cell $\mathbf{n} = (0, 0)$ colored in gray and *Inset* shows a full one-dimensional orbit through the configuration space when constraining the fold angle on an edge. Our randomly generated crease pattern admits six solutions to Eq. 15 and hence has three branches with strictly positive radii of curvature. There are three additional branches with identical strains and the oppositely signed curvatures.

of zero modes on an edge or interface beyond that predicted by local coordination number, which is known as topological polarization. The localization of these modes can be characterized by an inverse decay rate $\kappa_{1(2)} = -\text{Im}(q_{1(2)})$, where, e.g., $\kappa_2 < 0$ ($\kappa_2 > 0$) indicates the mode is exponentially localized on the bottom (top) edge as shown in Fig. 4A and B.

Since these states of self-stress can themselves be mapped onto zero modes via the duality discussed above for triangulated surfaces, whenever there is a zero mode at \mathbf{q} there must also be one at $-\mathbf{q}$, as shown by the pairing of inverse decay rates in Fig. 4A. This means that while it is always possible to impose a periodic distortion on a surface and, by the fundamental theorem of algebra, find a mode that exponentially decays into the bulk, the hidden symmetry guarantees that there is a corresponding mode on the opposing side. This shows polarization can never occur in Maxwell origami as observed by Chen et al. (47). In fact, the same work found Maxwell kirigami, composed of equal numbers of quadrilateral faces and holes, to topologically polarize is reconciled by a generalized version of the mechanical duality which pairs folding motions of the original structure with the self-stresses of a distinct structure obtained by replacing all faces with a hole and vice versa (59), thereby breaking the hidden symmetry.

Interestingly, this characteristic of Maxwell origami, while eliminating the Kane–Lubensky invariant, generates an additional topological property. The determinant of the compatibility matrix becomes a Laurent polynomial in the Bloch factors, $\det \mathbf{C}(\mathbf{q}) = \sum_{m,n} c_{mn} z_1^m z_2^n$, where the highest order of m and n is given by the total number of edges passing from the unit cell to the $\mathbf{n} = (1, 0)$ and $\mathbf{n} = (0, 1)$ cells, respectively, and c_{mn} are real coefficients determined by the crease geometry. This determinant vanishes at wavenumbers admitting zero modes, and previously it has been shown in two-dimensional (2D) Maxwell lattices (42) that the real and imaginary parts of the compatibility matrix generically vanish at zero-dimensional points within the 2D Brillouin zone. In the present case, the existence of zero modes at equal and opposite wavenumbers implies this determinant must be purely real so there instead appear one-dimensional lines of zero modes, as shown in Fig. 4A, corre-

sponding to the lines of magnetic waves observed in a quantum analog of origami sheets (54). Furthermore, the sign of the real compatibility matrix serves as a topological invariant which changes only when crossing such a line of zero modes as shown in Fig. 4C.

It is not clear how these linear modes extend into non-linear deformations. By mechanical criticality, a triangulated sheet with open boundaries must have modes due to the missing constraints at the edges. In general, though, the existence

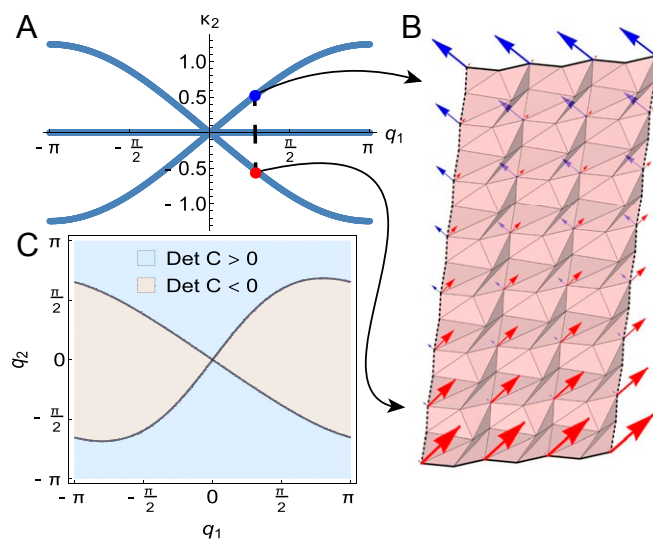


Fig. 4. (A) The signed inverse decay lengths, κ_2 , along the l_2 direction for zero modes at particular, real assignments of q_1 . The line along the origin corresponds to bulk zero modes that have zero inverse decay length everywhere. (B) The spatially periodic origami sheet shown in A with blue (red) arrows indicating zero mode vertex displacements on one vertex per cell (additional arrows omitted for visual clarity) that grow toward the top (bottom). (C) The determinant of the compatibility matrix for the origami sheet in B across the Brillouin zone.

of such finite-wavenumber modes is guaranteed only by continuous symmetries that are broken as the mode is extended nonlinearly. In particular, finite-wavenumber modes will induce sinusoidally varying amounts of Gaussian curvature through the sheet in contrast to the uniform folding motions that extend nonlinearly.

Conclusion

We have considered the rigid foldability of periodically triangulated origami with generic crease patterns and constructed a counting argument via Maxwell origami's combined mechanical duality and mechanical criticality. That argument shows translational and rotational rigid-body modes ensure the existence of folding motions that extend nonlinearly to yield two-dimensional spaces of rigidly foldable origami configurations which branch from the spatially periodic configuration. Furthermore, we showed this allows construction of crease patterns with a single degree of freedom simply by adding a single quadrilateral face to the unit cell. We leave for future work the refinement of our counting argument to address how discrete symmetries can permit nontriangulated patterns, such as the Miura-ori, to rigidly fold.

Finally, we have extended our counting argument to spatially varying modes, revealing that edge modes necessarily appear in pairs on opposite sides, explaining the lack of polarization previously observed (47). Our analysis reveals the existence of

one-dimensional lines of bulk zero modes in Maxwell origami, as opposed to zero-dimensional points, that could be used to reconfigure the origami sheet by introducing an expanded unit cell. This also identifies an additional topological invariant based on this hidden symmetry between folding motions and states of self-stress that may lead to additional topological properties (60). The generality of our results is unique in that it depends only on the coordination of the crease pattern rather than the specific geometry which may aid in the design of foldable materials in hard-to-control, microscopic environments.

Materials and Methods

We use Mathematica 12 to evolve our rigid origami. Each step of the trajectory first finds the tangent plane in the configuration space by computing the nullspace of the linear vertex condition. We then project the previous direction into this basis to minimize the change in our tangent vector at each step of the trajectory. Then, using Mathematica's *FindMinimum* function, we evolve our origami sheet in this direction, satisfying the vertex condition to numerical precision 10^{-16} using the Broyden–Fletcher–Goldfarb–Shanno QuasiNewton method.

Data Availability. There are no data underlying this work.

ACKNOWLEDGMENTS. B.G.-g.C. acknowledges funding from NSF Award PHY-1554887. C.D.S. acknowledges funding from NSF DMR-1822638. J.M. acknowledges funding from the Georgia Institute of Technology President's Fellowship and The Center for Science and Technology of Advanced Materials and Interfaces Graduate Student Fellowship.

1. E. Hawkes *et al.*, Programmable matter by folding. *Proc. Natl. Acad. Sci. U.S.A.* **107**, 12441–12445 (2010).
2. M. T. Tolley *et al.*, Self-folding origami: Shape memory composites activated by uniform heating. *Smart Mater. Struct.* **23**, 094006 (2014).
3. M. Z. Miskin *et al.*, Graphene-based bimorphs for micron-sized, autonomous origami machines. *Proc. Natl. Acad. Sci. U.S.A.* **115**, 466–470 (2018).
4. N. Bassik, G. M. Stern, D. H. Gracias, Microassembly based on hands free origami with bidirectional curvature. *Appl. Phys. Lett.* **95**, 091901 (2009).
5. Y. Liu, J. K. Boyles, J. Genzer, M. D. Dickey, Self-folding of polymer sheets using local light absorption. *Soft Matter* **8**, 1764–1769 (2012).
6. J. H. Na *et al.*, Programming reversibly self-folding origami with micropatterned photo-crosslinkable polymer trilayers. *Adv. Mater.* **27**, 79–85 (2015).
7. K. Miura, "Method of packaging and deployment of large membranes in space" in *The Institute of Space and Astronautical Science Report* (Japan Aerospace Exploration Agency, 1985), vol. 618, pp. 1–9.
8. K. Kuribayashi *et al.*, Self-deployable origami stent grafts as a biomedical application of Ni-rich TiNi shape memory alloy foil. *Mater. Sci. Eng. A* **419**, 131–137 (2006).
9. R. Tang *et al.*, Origami-enabled deformable silicon solar cells. *Appl. Phys. Lett.* **104**, 083501 (2014).
10. Z. Song *et al.*, Origami lithium-ion batteries. *Nat. Commun.* **5**, 3140 (2014).
11. J. Ma, Z. You, The origami crash box. *Origami* **5**, 277–290 (2011).
12. X. Liu, S. Yao, B. S. Cook, M. M. Tentzeris, S. V. Georgakopoulos, An origami reconfigurable axial-mode bifilar helical antenna. *IEEE Trans. Antenn. Propag.* **63**, 5897–5903 (2015).
13. L. Mahadevan, S. Rica, Self-organized origami. *Science* **307**, 1740 (2005).
14. H. Akitaya *et al.*, Rigid foldability is NP-hard. arXiv:1812.01160 (4 December 2018).
15. B. Sarah-Marie, T. C. Hull, Modelling the folding of paper into three dimensions using affine transformations. *Lin. Algebra Appl.* **348**, 273–282 (2002).
16. B. Liu *et al.*, Topological kinematics of origami metamaterials. *Nat. Phys.* **14**, 811–815 (2018).
17. S. Waitukaitis, R. Menaut, B. G. Chen, M. van Hecke, Origami multistability: From single vertices to metasheets. *Phys. Rev. Lett.* **114**, 055503 (2015).
18. M. Stern, M. B. Pinson, A. Murugan, The complexity of folding self-folding origami. *Phys. Rev. X* **7**, 041070 (2017).
19. B. Gg. Chen, C. D. Santangelo, Branches of triangulated origami near the unfolded state. *Phys. Rev. X* **8**, 011034 (2018).
20. M. Berry, M. Lee-Trimble, C. Santangelo, Topological transitions in the configuration space of non-Euclidean origami. arXiv:1910.01008 (2 October 2019).
21. J. L. Silverberg *et al.*, Using origami design principles to fold reprogrammable mechanical metamaterials. *Science* **345**, 647–650 (2014).
22. J. L. Silverberg *et al.*, Origami structures with a critical transition to bistability arising from hidden degrees of freedom. *Nat. Mater.* **14**, 389–393 (2015).
23. Z. Y. Wei, Z. V. Guo, L. Dudte, H. Y. Liang, L. Mahadevan, Geometric mechanics of periodic pleated origami. *Phys. Rev. Lett.* **110**, 215501 (2013).
24. M. Schenk, S. D. Guest, Geometry of Miura-folded metamaterials. *Proc. Natl. Acad. Sci. U.S.A.* **110**, 3276–3281 (2013).
25. C. Lv, D. Krishnaraju, G. Konjevod, H. Yu, H. Jiang, Origami based mechanical metamaterials. *Sci. Rep.* **4**, 5979 (2014).
26. H. Nassar, A. Lebé, L. Monasse, Curvature, metric and parametrization of origami tessellations: Theory and application to the eggbox pattern. *Proc. Math. Phys. Eng. Sci.* **473**, 20160705 (2017).
27. P. P. Pratapa, K. Liu, G. H. Paulino, Geometric mechanics of origami patterns exhibiting Poisson's ratio switch by breaking mountain and valley assignment. *Phys. Rev. Lett.* **122**, 155501 (2019).
28. E. T. Filipov, T. Tachi, G. H. Paulino, Origami tubes assembled into stiff, yet reconfigurable structures and metamaterials. *Proc. Natl. Acad. Sci. U.S.A.* **112**, 12321–12326 (2015).
29. A. A. Evans, J. L. Silverberg, C. D. Santangelo, Lattice mechanics of origami tessellations. *Phys. Rev.* **92**, 013205 (2015).
30. S. Waitukaitis, M. van Hecke, Origami building blocks: Generic and special four-vertices. *Phys. Rev.* **93**, 023003 (2016).
31. P. Dieleman, N. Vasmel, S. Waitukaitis, M. van Hecke, Jigsaw puzzle design of pluripotent origami. *Nat. Phys.* **16**, 63–68 (2019).
32. M. B. Pinson *et al.*, Self-folding origami at any energy scale. *Nat. Commun.* **8**, 15477 (2017).
33. H. Gluck, "Almost all simply connected closed surfaces are rigid" in *Geometric Topology*, L. C. Glaser, T. B. Rushing, eds. (Springer, 1975), pp. 225–239.
34. T. Tachi, Rigid folding of periodic origami tessellations. *Origami* **6**, 97–108 (2015).
35. M. Schenk, S. D. Guest, "Origami folding: A structural engineering approach" in *Origami 5: Fifth International Meeting of Origami Science, Mathematics, and Education*, P. Wang-Iverson, R. J. Lang, M. Yim, Eds. (CRC Press, Boca Raton, FL, 2011), pp. 291–304.
36. E. Filipov, K. Liu, T. Tachi, M. Schenk, G. Paulino, Bar and hinge models for scalable analysis of origami. *Int. J. Solid Struct.* **124**, 26–45 (2017).
37. T. Lubensky, C. Kane, X. Mao, A. Souslov, K. Sun, Phonons and elasticity in critically coordinated lattices. *Rep. Prog. Phys.* **78**, 073901 (2015).
38. X. Mao, T. C. Lubensky, Maxwell lattices and topological mechanics. *Annu. Rev. Condens. Matter Phys.* **9**, 413–433 (2018).
39. S. Guest, J. Hutchinson, On the determinacy of repetitive structures. *J. Mech. Phys. Solid.* **51**, 383–391 (2003).
40. C. S. Borcea, I. Streinu, Periodic frameworks and flexibility. *Proc. Math. Phys. Eng. Sci.* **466**, 2633–2649 (2010).
41. C. Kane, T. Lubensky, Topological boundary modes in isostatic lattices. *Nat. Phys.* **10**, 39 (2014).
42. D. Z. Rocklin, B. G. Chen, M. Falk, V. Vitelli, T. Lubensky, Mechanical Weyl modes in topological Maxwell lattices. *Phys. Rev. Lett.* **116**, 135503 (2016).
43. D. Z. Rocklin, Directional mechanical response in the bulk of topological metamaterials. *New J. Phys.* **19**, 065004 (2017).
44. D. Z. Rocklin, S. Zhou, K. Sun, X. Mao, Transformable topological mechanical metamaterials. *Nat. Commun.* **8**, 14201 (2017).
45. H. Crapo, W. Whiteley, Statics of frameworks and motions of panel structures: A projective geometric introduction. *Struct. Topol.* **1982**, 6 (1982).

46. T. Tachi, Design of infinitesimally and finitely flexible origami based on reciprocal figures. *J. Geom. Graph.* **16**, 223–234 (2012).
47. B. G. Chen et al., Topological mechanics of origami and kirigami. *Phys. Rev. Lett.* **116**, 135501 (2016).
48. F. Feng, P. Plucinsky, R. D. James, Helical Miura origami. *Phys. Rev. E* **101**, 033002 (2020).
49. J. C. Maxwell, L. on the calculation of the equilibrium and stiffness of frames. *Lond. Edinb. Dublin Philos. Mag. J. Sci.* **27**, 294–299 (1864).
50. C. Calladine, Buckminster Fuller's "tensegrity" structures and Clerk Maxwell's rules for the construction of stiff frames. *Int. J. Solid Struct.* **14**, 161–172 (1978).
51. T. Tachi, Simulation of rigid origami. *Origami* **4**, 175–187 (2009).
52. S. Guest, P. Fowler, Symmetry-extended counting rules for periodic frameworks. *Philos. Trans. Math. Phys. Eng. Sci.* **372**, 20120029 (2014).
53. J. Harris, *Algebraic Geometry: A First Course* (Springer Science & Business Media, 2013), vol. 133.
54. K. Roychowdhury, D. Z. Rocklin, M. J. Lawler, Topology and geometry of spin origami. *Phys. Rev. Lett.* **121**, 177201 (2018).
55. Z. Gong et al., Topological phases of non-Hermitian systems. *Phys. Rev. X* **8**, 031079 (2018).
56. E. Shender, V. Cherepanov, P. Holdsworth, A. Berlinsky, Kagomé antiferromagnet with defects: Satisfaction, frustration, and spin folding in a random spin system. *Phys. Rev. Lett.* **70**, 3812 (1993).
57. P. Chandra, P. Coleman, I. Ritchey, The anisotropic kagome antiferromagnet: A topological spin glass? *J. Phys.* **3**, 591–610 (1993).
58. I. Ritchey, P. Chandra, P. Coleman, Spin folding in the two-dimensional Heisenberg kagomé antiferromagnet. *Phys. Rev. B* **47**, 15342 (1993).
59. W. Finbow, E. Ross, W. Whiteley, The rigidity of spherical frameworks: Swapping blocks and holes. *SIAM J. Discrete Math.* **26**, 280–304 (2012).
60. K. Roychowdhury, M. J. Lawler, Classification of magnetic frustration and metamaterials from topology. *Phys. Rev. B* **98**, 094432 (2018).

1

2 **Supplementary Information for**

3 **Hidden symmetries generate rigid folding mechanisms in periodic origami SI Appendix**

4 **James McInerney, Bryan Chen, Louis Theran, Christian Santangelo, Zeb Rocklin**

5 **Corresponding Author name.**

6 **E-mail: author.two@email.com**

7 **This PDF file includes:**

8 Supplementary text

9 Legends for Movies S1 to S2

10 **Other supplementary materials for this manuscript include the following:**

11 Movies S1 to S2

12 Supporting Information Text

13 1. Vertex and loop constraints

14 Here we provide a proof of the Belcastro-Hull vertex constraint for generic vertices. Let us condense our notation from the
 15 main text and label the N_e edges leaving a vertex as \hat{r}_i for i taking integer values from 1 to N_e . We similarly denote the
 16 normal vectors on each face as \hat{n}_i , where the i th face precedes the i th edge. Then taking $\hat{r}_1 = \hat{x}$ and $\hat{n}_1 = \hat{z}$, the rotation
 17 $\mathbf{P}_1 = \mathbf{R}_z(\alpha_1)\mathbf{R}_x(\rho_1)$ defines the similarity transform that rotates the coordinate basis to $\hat{r}_2 = \hat{x}$ and $\hat{n}_2 = \hat{z}$ via $\mathbf{P}_1^{-1}\hat{r}_1\mathbf{P}_1 = \hat{r}_2$
 18 and $\mathbf{P}_1^{-1}\hat{n}_1\mathbf{P}_1 = \hat{n}_2$. Now suppose we are at the i th edge and have found a similarity transform such that $\hat{r}_i = \hat{x}$ and $\hat{n}_i = \hat{z}$.
 19 Then the rotation $\mathbf{P}_i = \mathbf{R}_z(\alpha_i)\mathbf{R}_x(\rho_i)$ defines the similarity transform that rotates the coordinate basis to $\hat{r}_{i+1} = \hat{x}$ and
 20 $\hat{n}_{i+1} = \hat{z}$ via $\mathbf{P}_i^{-1}\hat{r}_i\mathbf{P}_i = \hat{r}_{i+1}$ and $\mathbf{P}_i^{-1}\hat{n}_i\mathbf{P}_i = \hat{n}_{i+1}$. Hence for any edge we can define the similarity transform $\chi_i = \prod_{i'=1}^i \mathbf{P}_{i'}$
 21 to rotate the initial edge and face normals to the i th edge and face normals $\hat{r}_i = \chi_i^{-1}\hat{r}_1\chi_i$ and $\hat{n}_i = \chi_i^{-1}\hat{n}_1\chi_i$. Since we have
 22 chosen $\hat{r}_1 = \hat{x}$ and $\hat{n}_1 = \hat{z}$, we must have $\chi_i = \mathbf{I}$ for a closed loop around the vertex yielding

$$23 \quad \mathbf{F}_i = \prod_{(i,j)} \mathbf{R}_z(\alpha_{(i,j,k)})\mathbf{R}_x(\rho_{(i,j)}) = \mathbf{I}, \quad [1]$$

24 after returning subscripts as in the main text.

25 2. Cylindrical surfaces from periodic origami sheets

26 Here we show how inter-cell orientation and position compatibility,

$$\mathbf{S}_1\mathbf{S}_2 = \mathbf{S}_2\mathbf{S}_1, \quad [2]$$

$$\mathbf{l}_1 + \mathbf{S}_1\mathbf{l}_2 = \mathbf{l}_2 + \mathbf{S}_2\mathbf{l}_1, \quad [3]$$

27 can be used to define a continuous cylinder. First, we fix the two lattice rotation matrices, $\mathbf{S}_{1,2}$, to be rotations about the \hat{s}
 28 axis to enforce orientation compatibility, Eqn. 2. It immediately follows the projection of position compatibility, Eqn. 3, along
 29 this rotation axis is trivially satisfied. We then examine the components transverse to \hat{s} denoted by the superscript \perp

$$30 \quad \mathbf{l}_1^\perp + \mathbf{S}_1^\perp\mathbf{l}_2^\perp = \mathbf{l}_2^\perp + \mathbf{S}_2^\perp\mathbf{l}_1^\perp. \quad [4]$$

31 Here, $\mathbf{S}_{1,2}^\perp$ denote two-dimensional rotation matrices which map transverse vectors to transverse vectors so Eqn. 4 is invertible,
 32 requiring the lattice vectors satisfy

$$33 \quad \mathbf{l}_2^\perp = (\mathbf{1} - \mathbf{S}_1^\perp)^{-1}(\mathbf{1} - \mathbf{S}_2^\perp)\mathbf{l}_1^\perp. \quad [5]$$

34 Since we can always choose a Cartesian basis which has one axis along \hat{s} and another along \mathbf{l}_1^\perp , Eqns. 2 and 3 imply our lattice
 35 is specified by the five-parameter family of $\{\theta_1, \theta_2, |\mathbf{l}_1^\perp|, \mathbf{l}_1 \cdot \hat{s}, \mathbf{l}_2 \cdot \hat{s}\}$.

36 Now suppose we would like to define a cylinder which intersects the first vertex in every cell. Clearly, this cylinder's
 37 symmetry axis must lie along the origami's axis of rotation. To obtain its radius, we again consider the projection of the
 38 surface into the plane defined by this axis. This surface connects the first vertex of the unit cell with its counterpart in the
 39 neighboring cells by a planar curve. The transverse lattice vectors, $\mathbf{l}_{1,2}^\perp$, are then the geometric chords of this curve which
 40 subtend the corresponding rotation angle, $\theta_{1,2}$. This allows us to write the planar curve's radius

$$41 \quad r = \frac{|\mathbf{l}_{1,2}^\perp|}{2 \sin(\theta_{1,2}/2)}. \quad [6]$$

42 Furthermore, the dependence between the two lattice vectors shows $|\mathbf{l}_2^\perp| = |\mathbf{l}_1^\perp| \csc(\theta_1/2) \sin(\theta_2/2)$ so that this radius is indeed
 43 unique. Hence our periodic origami sheets can be used to define a continuous cylinder whose symmetry axis is given by \hat{s} and
 44 whose radius of curvature is given by $\kappa = 1/r$ from Eqn. 6. Since the sign of this term depends on the definition of the rotation
 45 axis, we define a more robust notion of direction via $\text{sign}(\kappa) = \text{sign}\left(\mathbf{S}_1\mathbf{l}_2 \cdot (\mathbf{l}_1 \times \mathbf{l}_2)\right) \text{sign}\left(\theta_2\right) = \text{sign}\left(\mathbf{S}_2\mathbf{l}_1 \cdot (\mathbf{l}_1 \times \mathbf{l}_2)\right) \text{sign}\left(\theta_1\right)$.

46 3. Screw-periodic vertex positions

47 Here, we show how to compute vertex positions in a screw-periodic lattice. Given the position of each vertex in the unit cell,
 48 denoted by \mathbf{r}_i , we can compute the position of an arbitrary vertex by summation of all edge vectors traveled along to reach it
 49 via

$$50 \quad \mathbf{r}_i(\mathbf{n}) = \sum_{n'=0}^{n_1-1} \mathbf{S}_1^{n'}\mathbf{l}_1 + \mathbf{S}_1^{n_2} \sum_{n'=0}^{n_1-1} \mathbf{S}_2^{n'}\mathbf{l}_2 + \mathbf{S}_1^{n_1} \mathbf{S}_2^{n_2} \mathbf{r}_i. \quad [7]$$

The rotation matrices can be summed component-wise since any rotation matrix satisfies $\mathbf{S}^n(\theta) = \mathbf{S}(n\theta)$. Without loss of generality, let us take $\hat{s} = \hat{z}$. We can then rewrite the terms $\cos(n\theta)$ and $\sin(n\theta)$ using Euler's formula and simply sum the exponents of complex numbers $\sum_{n'=0}^{n-1} w^{n'} = \frac{1-w^n}{1-w}$. After simplification we have

$$\begin{aligned}\bar{\mathbf{S}}(n) &\equiv \sum_{n'=0}^{n-1} \mathbf{S}^{n'} = \begin{bmatrix} \overline{\cos}(n\theta) & -\overline{\sin}(n\theta) & 0 \\ \overline{\sin}(n\theta) & \overline{\cos}(n\theta) & 0 \\ 0 & 0 & n \end{bmatrix}, \\ \overline{\cos}(n\theta) &\equiv \sum_{n'=0}^{n-1} \cos(n\theta) = \frac{1}{2} \left(1 - \cos(n\theta) + \cos\left(\frac{\theta}{2}\right) \sin(n\theta) \right), \\ \overline{\sin}(n\theta) &\equiv \sum_{n'=0}^{n-1} \sin(n\theta) = \frac{1}{2} \left(\cos\left(\frac{\theta}{2}\right) - \cos\left(\frac{\theta}{2} - n\theta\right) \right) \csc\left(\frac{\theta}{2}\right),\end{aligned}\tag{8}$$

51 where we drop the subscripts for readability.

52 4. Linear vertex constraint

53 Here, we perform a first-order expansion of the Belcastro-Hull vertex condition,

$$\mathbf{F}_i = \prod_{(i,j)} \mathbf{R}_z(\alpha_{(i,j,k)}) \mathbf{R}_x(\rho_{(i,j)}) = \mathbf{I},\tag{9}$$

55 to construct the linear vertex constraint in agreement with the main text. Consider an infinitesimal change to the fold angles
56 $\rho_{(i,j)} \rightarrow \rho_{(i,j)} + \phi_{(i,j)}$ where each $|\phi_{(i,j)}| \ll 1$. The rotation matrix $\mathbf{R}_x(\rho_{(i,j)})$ then becomes $(\mathbf{I} + \phi_{(i,j)} \boldsymbol{\sigma}_x) \mathbf{R}_x(\rho_{(i,j)})$ where $\boldsymbol{\sigma}_x$
57 is the infinitesimal generator of rotations about the x -axis. Expanding the product around vertex i to first-order yields a sum
58 of products where each term with coefficient $\phi_{(i,j)}$ shifts the location of $\boldsymbol{\sigma}_x$ so that it lies on the left of $\mathbf{R}_x(\rho_{(i,j)})$. To the left
59 of this rotation generator is the product $\left(\prod_{(i',j')}^{(i,j-1)} \mathbf{R}_z(\alpha_{(i',j',k')}) \mathbf{R}_x(\rho_{(i',j')}) \right) \mathbf{R}_z(\alpha_{(i,j-1,k)})$ where we use $(i, j-1)$ to denote
60 the face-sharing edge clockwise to (i, j) . As in the construction above of Eqn. 9, this is simply the similarity transform, \mathbf{P}_j ,
61 that maps \hat{x} to $\hat{r}_{(i,j)}$. Moreover, since the fold angle assignment satisfies the Belcastro-Hull vertex condition the product
62 to the right of $\boldsymbol{\sigma}_x$ is exactly the inverse of this similarity transformation. Hence, the sum over these products of rotations
63 become a sum over infinitesimal rotations about $\hat{r}_{(i,j)}$. Then, using the skew-symmetry of these infinitesimal rotations we are
64 able to rewrite the linear vertex constraint as given in the main text Eqn. 13. Note, however, we are only able to choose the
65 direction of one edge and one face within the sheet to lie along the Cartesian basis vectors. Hence, this condition can vary by
66 some rotation acting uniformly on each unit vector for the remaining vertices. This has no effect on the solutions, $\phi_{(i,j)}$, which
67 satisfy the condition, but changes the basis in which the left nullspace (vertex zero modes) is written.

68 5. Quadratic vertex constraint

69 Here, we perform a second-order expansion of the Belcastro-Hull vertex condition, Eqn. 9, to construct the quadratic vertex
70 constraint in agreement with the main text. Expanding $\mathbf{R}_x(\rho_{(i,j)})$ to second order adds an extra term $(\mathbf{I} + \phi_{(i,j)} \boldsymbol{\sigma}_x +$
71 $\frac{1}{2} \phi_{(i,j)}^2 \boldsymbol{\tau}_x) \mathbf{R}_x(\rho_{(i,j)})$ for

$$\boldsymbol{\tau}_x \equiv \begin{bmatrix} 0 & 0 & 0 \\ 0 & -1 & 0 \\ 0 & 0 & -1 \end{bmatrix}.\tag{10}$$

Then expanding the Belcastro-Hull vertex condition and again using the fact that finite rotations perform a similarity transform
mapping the x -axis onto the relevant edge vector, we obtain the sum $\sum_{(i,j)} \sum_{(i,k); k>j} \phi_{(i,j)} \phi_{(i,k)} \boldsymbol{\sigma}_{(i,j)} \boldsymbol{\sigma}_{(i,k)} + \frac{1}{2} \sum_{(i,j)} \phi_{(i,j)}^2 \boldsymbol{\tau}_{(i,j)} =$
0. This simplifies considerably using bra-ket notation to

$$\sum_{(i,j)} \sum_{\substack{(i,k) \\ k>j}} \phi_{(i,j)} \phi_{(i,k)} \left(|\mathbf{r}_{(i,j)}\rangle \langle \mathbf{r}_{(i,k)}| - \langle \mathbf{r}_{(i,j)} | \mathbf{r}_{(i,k)} \rangle \mathbf{I} \right) + \frac{1}{2} \sum_{(i,j)} \phi_{(i,j)}^2 \left(|\mathbf{r}_{(i,j)}\rangle \langle \mathbf{r}_{(i,j)}| - \mathbf{I} \right) = \mathbf{0},\tag{11}$$

73 using $k > j$ to signify edges (i, k) always follow counter-clockwise to edge (i, j) . We can then consider diagonal and off-diagonal
74 components of this matrix constraint separately by introducing superscripts μ, ν to denote components of the edge vectors.

Along the diagonal $\mu = \nu$ and the first sum is equivalent to

$$\begin{aligned}\sum_{(i,j)} \sum_{\substack{(i,k) \\ k>j}} \phi_{(i,j)} \phi_{(i,k)} \left(|\mathbf{r}_{(i,j)}^\mu\rangle \langle \mathbf{r}_{(i,k)}^\mu| - \langle \mathbf{r}_{(i,j)}^\mu | \mathbf{r}_{(i,k)}^\mu \rangle \right) &= \frac{1}{2} \left(\sum_{(i,j)} \sum_{(i,k)} \phi_{(i,j)} \phi_{(i,k)} \left(|\mathbf{r}_{(i,j)}^\mu\rangle \langle \mathbf{r}_{(i,k)}^\mu| - \langle \mathbf{r}_{(i,j)}^\mu | \mathbf{r}_{(i,k)}^\mu \rangle \right) \right. \\ &\quad \left. - \frac{1}{2} \sum_{(i,j)} \phi_{(i,j)}^2 \left(|\mathbf{r}_{(i,j)}^\mu\rangle \langle \mathbf{r}_{(i,j)}^\mu| - 1 \right) \right).\end{aligned}\tag{12}$$

75 The double summation of the first term can be computed independently which then necessarily vanishes when the $\phi_{(i,j)}$ satisfy
 76 the linear vertex condition

$$77 \quad \sum_{(i,j)} \phi_{(i,j)}(\mathbf{n}) \hat{\mathbf{r}}_{(i,j)}(\mathbf{n}) = \mathbf{0}. \quad [13]$$

78 The single summation exactly cancels the second term of Eqn. 11 implying the diagonal automatically vanishes for linear
 79 folding motions.

The off-diagonal components are not trivially satisfied, but they can be simplified into the form given the main text. We again rewrite the double-summation

$$\begin{aligned} \sum_{(i,j)} \sum_{\substack{(i,k) \\ k>j}} \phi_{(i,j)} \phi_{(i,k)} |\mathbf{r}_{(i,j)}^\mu\rangle \langle \mathbf{r}_{(i,k)}^\nu| &= \sum_{(i,j)} \sum_{(i,k)} \phi_{(i,j)} \phi_{(i,k)} |\mathbf{r}_{(i,j)}^\mu\rangle \langle \mathbf{r}_{(i,k)}^\nu| \\ &- \sum_{(i,j)} \sum_{\substack{(i,k) \\ k>j}} \phi_{(i,j)} \phi_{(i,k)} |\mathbf{r}_{(i,j)}^\nu\rangle \langle \mathbf{r}_{(i,j)}^\mu| - \sum_{(i,j)} \phi_{(i,j)}^2 |\mathbf{r}_{(i,j)}^\mu\rangle \langle \mathbf{r}_{(i,j)}^\nu|. \end{aligned} \quad [14]$$

80 Similarly to the diagonal components, the first double-sum vanishes for linear folding motions that satisfy Eqn. 13. Adding the
 81 remaining term in Eqn. 11 reveals this constraint is skew-symmetric. It is hence satisfied when the difference with its transpose
 82 vanishes which is exactly the cross product definition

$$83 \quad \sum_{(i,j)} \sum_{\substack{(i,k) \\ k>j}} \phi_{(i,j)} \phi_{(i,k)} \hat{\mathbf{r}}_{(i,j)} \times \hat{\mathbf{r}}_{(i,k)} = \mathbf{0}. \quad [15]$$

84 Finally, since $\phi_{(i,j)}$ satisfy the linear vertex condition we have $\sum_{k>j} \phi_{(i,k)} \hat{\mathbf{r}}_{(i,k)} = -\sum_{k<j} \phi_{(i,k)} \hat{\mathbf{r}}_{(i,k)}$ so this may be rewritten
 85 as given in the main text

$$86 \quad \sum_{(i,j)} \delta \phi_{(i,j)} \hat{\mathbf{r}}_{(i,j)} + \sum_{(i,j)} \phi_{(i,j)} \left(\sum_{\substack{(i,k) \\ k<j}} \phi_{(i,k)} \hat{\mathbf{r}}_{(i,k)} \right) \times \hat{\mathbf{r}}_{(i,j)} = \mathbf{0}. \quad [16]$$

87 The interior sum gives the angular velocity $\boldsymbol{\omega}_{(i,j,j')} - \boldsymbol{\omega}_{(i,i_1,i_2)}$ so that the quadratic term gives the sum over changes in
 88 orientation of unit vectors $\hat{\mathbf{r}}_{(i,j)}$ with the face (i, i_1, i_2) fixed. However, as stated in the main text, since the $\phi_{(i,j)}$ satisfy the
 89 linear vertex equation, Eqn. 13, we can add the constant $\boldsymbol{\omega}_{(i,i_1,i_2)} - \boldsymbol{\omega}_{(1,2,3)}$ to Eqn. 16 at every vertex without changing the
 90 result. Hence, the quadratic term is equivalent to summing over the changes in edge directions $\sum_{(i,j)} \delta \hat{\mathbf{r}}_{(i,j)} \phi_{(i,j)}$.

91 6. Second-order folding motions via mechanical duality

92 As discussed in the main text and the previous appendix, second-order folding motions $\delta \phi_{(i,j)}$ exist provided that they satisfy
 93 the following relation to the first-order motions $\phi_{(i,j)}$

$$94 \quad \sum_{(i,j)} \delta \phi_{(i,j)} \hat{\mathbf{r}}_{(i,j)} + \sum_{(i,j)} \phi_{(i,j)} \left(\sum_{\substack{(i,k) \\ k<j}} \phi_{(i,k)} \hat{\mathbf{r}}_{(i,k)} \right) \times \hat{\mathbf{r}}_{(i,j)} = \mathbf{0} \quad [17]$$

95 at every vertex i in the unit cell. This first sum can, as discussed in the main text, be expressed as the vector $\mathbf{Q} \delta \phi$. At first
 96 appearance, it might seem that regardless of the first-order contributions a second-order correction can be chosen to satisfy the
 97 second order corrections. However, the equilibrium matrix is not invertible, so the additional term cannot have any contribution
 98 that lies in its left nullspace. Hence, a sufficient condition for the existence of the second-order correction to exist is that the
 99 double sum above not lie in the left nullspace of the equilibrium matrix, which is also the right nullspace of the compatibility
 100 matrix. Starting from a spatially periodic configuration, that consists solely of the three Euclidean translations. The resultant
 101 condition is then simply that the above quadratic condition vanish when summed over each vertex in the unit cell:

$$102 \quad \sum_i \sum_{(i,j)} \sum_{\substack{(i,k) \\ k<j}} \phi_{(i,j)} \phi_{(i,k)} \hat{\mathbf{r}}_{(i,k)} \times \hat{\mathbf{r}}_{(i,j)} = \mathbf{0}. \quad [18]$$

103 Now, we may show by induction that this sum over every vertex in the interior of the unit cell may be reduced to a sum
 104 over a loop drawn around the boundary of the unit cell. Suppose that this relationship already holds true for a certain loop, as
 105 it certainly does for a loop around a single vertex, when the two scenarios are the same. Suppose that we add a single adjacent
 106 vertex i' . In the above equation, this would increase the total sum by an amount

$$107 \quad \sum_{(i',j)} \sum_{\substack{(i',k) \\ k<j}} \phi_{(i',j)} \phi_{(i',k)} \hat{\mathbf{r}}_{(i',k)} \times \hat{\mathbf{r}}_{(i',j)}. \quad [19]$$

108 The loop sum, on the other hand, would instead be increased by an amount

$$109 \sum_{(i',j)} \sum_{\substack{(i',k) \\ k < j}} \pm \phi_{(i',j)} \phi_{(i',k)} \hat{\mathbf{r}}_{(i',k)} \times \hat{\mathbf{r}}_{(i',j)} + \sum_{(i'',j'')} \sum_{(i',j)} \pm \phi_{(i'',j'')} \phi_{(i',j)} \hat{\mathbf{r}}_{(i'',j'')} \times \hat{\mathbf{r}}_{(i',j)}. \quad [20]$$

110 Here, the \pm is positive when a new edge has been crossed due to the addition of the new vertex and negative for an edge
 111 that has been removed from the outer loop as it winds around the new vertex. The second sum, over every edge of the new
 112 vertex and every edge that precedes it in the loop, may be eliminated, and the first sum may be transformed into that of the
 113 previous equation, by noting that because the first-order conditions are satisfied then $\sum_{(i,j)} \phi_{(i,j)} \hat{\mathbf{r}}_{(i,j)} = 0$ at every vertex.

114 In this way, the second-order conditions may be satisfied provided that the first-order conditions satisfy

$$\sum_{(i,j)} \sum_{(i',j')} \phi_{(i,j)} \phi_{(i',j')} \hat{\mathbf{r}}_{(i,j)} \times \hat{\mathbf{r}}_{(i',j')} = 0, \quad [21]$$

115 where now the sum is over ordered pairs of edges encountered on a loop drawn counter-clockwise around the unit cell.

116 However, such a loop may also be decomposed as successive paths along the first lattice direction, the second lattice direction,
 117 the reverse of the first lattice direction and the reverse of the second lattice direction. Expressed in terms of the lattice rotations,
 118 this is simply the second-order expansion of

$$\mathbf{S}_1 \mathbf{S}_2 \mathbf{S}_1^{-1} \mathbf{S}_2^{-1} = \mathbf{I}. \quad [22]$$

119 Hence, we find that any set of linear folding motions may be extended to second-order if and only if it satisfies orientation
 120 compatibility to second-order. As discussed in the main text, flat vertices enlarge the left nullspace of the equilibrium
 121 matrix and generate both additional linear modes and additional constraints, therefore leading to more complicated but not
 122 higher-dimensional sets of rigid folding motions.

123 7. Vertex displacements from folding motions

124 Here, we evaluate the double-summation that maps from linear folding motions to vertex displacements with the face $(1, 2, 3)$
 125 of cell $\mathbf{n} = (0, 0)$ held fixed. The angular velocity of face (i, j, k) in cell \mathbf{n} is given by the sum $\boldsymbol{\omega}_{(i,j,k)}(\mathbf{n}) = \sum_{(i',j')} \phi_{(i',j')} \hat{\mathbf{r}}_{(i',j')}$
 126 where (i', j') takes on the value for each edge which is passed on a path from the initial face to face (i, j, k) in cell \mathbf{n} . Since our
 127 folding motions are uniform and the edge vectors are screw-periodic, we can expand this sum as

$$128 \boldsymbol{\omega}_{(i,j,k)}(\mathbf{n}) = \bar{\mathbf{S}}_1(n_1) \boldsymbol{\Omega}_1 + \mathbf{S}_1^{n_1} \bar{\mathbf{S}}_2(n_2) \boldsymbol{\Omega}_2 + \mathbf{S}_1^{n_1} \mathbf{S}_2^{n_2} \boldsymbol{\omega}_{(i,j,k)}, \quad [23]$$

129 using $\boldsymbol{\omega}_{(i,j,k)}$ to denote the angular velocity of face (i, j, k) in the unit cell and and $\boldsymbol{\Omega}_{1,2} = \sum_{1,2} \hat{\mathbf{r}}_{(i,j)} \phi_{(i,j)}$ denote the cell
 130 angular velocities computed by summing along the path from face $(1, 2, 3)$ of the $\mathbf{n} = (0, 0)$ cell to the same face in the
 131 $\mathbf{n} = (1, 0)$ and $\mathbf{n} = (0, 1)$ cells respectively. These cell angular velocities, $\boldsymbol{\Omega}_{1,2}$, give the components of the skew-symmetric
 132 matrices $\delta \mathbf{S}_{1,2}$ introduced in the main text. Furthermore, Eqn. 23 is independent of the order of summation since the angular
 133 velocities, $\boldsymbol{\omega}_{(i,j,k)}$, are construction from linear folding motions, $\phi_{(i,j)}$, that satisfy Eqn. 13. The displacement of vertex k in cell
 134 \mathbf{n} is $\mathbf{u}_k(\mathbf{n}) = \sum_{(i',j',k')}^k \left(\sum_{(i'',j'',k'')} \phi_{(i'',j'')} \hat{\mathbf{r}}_{(i'',j'')} \right) \times \mathbf{r}_{(i',k')}$ which we now evaluate for spatially periodic and screw-periodic
 135 configurations.

First, consider a flat (not necessarily developable) configuration in which $\mathbf{r}_{(i,k)}(\mathbf{n}) = \mathbf{r}_{(i,k)}$ so that the periodicity is
 described as would be for a conventional crystal. The angular velocity of a face in this configuration reduces to $\boldsymbol{\omega}_{(i,j,k)}(\mathbf{n}) =$
 $n_1 \boldsymbol{\Omega}_1 + n_2 \boldsymbol{\Omega}_2 + \boldsymbol{\omega}_{(i,j,k)}$. The displacement of a vertex can be expanded as

$$\begin{aligned} \mathbf{u}_k(\mathbf{n}) &= n_1 \sum_{(i',j',k')}^{n_1=1} \boldsymbol{\omega}_{(i',j',k')} \times \mathbf{r}_{(i',k')} + n_2 \sum_{(i',j',k')}^{n_2=1} \boldsymbol{\omega}_{(i',j',k')} \times \mathbf{r}_{(i',k')} \\ &\quad + \frac{n_1(n_1+1)}{2} \boldsymbol{\Omega}_1 \times \mathbf{l}_1 + \frac{n_2(n_2+1)}{2} \boldsymbol{\Omega}_2 \times \mathbf{l}_2 + n_1 n_2 \boldsymbol{\Omega}_1 \times \mathbf{l}_2, \end{aligned} \quad [24]$$

where the last term is equivalent to $n_2 n_1 \boldsymbol{\Omega}_2 \times \mathbf{l}_1$ by since the linear folding motions satisfy the expansion of position compatibility,
 Eqn. 3, to first-order. The first two terms, which are linear in n , can be interpreted as intracell strains while the last three
 terms, which are quadratic in n , characterize intercell curvatures. Hence, the accumulation of cell angular velocities, $\boldsymbol{\Omega}_{1,2}$,
 gives rise to the cylindrical structure from the flat state. For this reason we define the following quantities

$$\delta \mathbf{l}_{1,2} \equiv \sum_{(i',j',k')}^{n_{1,2}=1} \boldsymbol{\omega}_{(i',j',k')} \times \mathbf{r}_{(i',k')}, \quad [25]$$

$$\delta \kappa_{11,22}^{-1} \equiv \boldsymbol{\Omega}_{1,2} \times \mathbf{l}_{1,2}, \quad [26]$$

$$\delta \kappa_{12}^{-1} \equiv \boldsymbol{\Omega}_1 \times \mathbf{l}_2 = \delta \kappa_{21}^{-1} \equiv \boldsymbol{\Omega}_2 \times \mathbf{l}_1, \quad [27]$$

136 for changes to the lattice vectors $\delta\mathbf{l}_{1,2}$ and changes to the curvatures $\delta\kappa_{ij}$. Moreover, $\mathbf{\Omega}_{1,2} = \mathbf{0}$ implies there is no curvature
 137 in the corresponding lattice direction so that it either defines the rotation axis or the sheet remains flat. This occurs for the
 138 planar folding motions of crease patterns such as the Miura-ori and the eggbox.

More generally, we can perform the double summation for cylindrical origami. In this case, the face angular velocities take
 the form given in Eqn. 23 and the edge vectors take the form $\mathbf{r}_{(i,j)}(\mathbf{n}) = \mathbf{S}_1^{n_1} \mathbf{S}_2^{n_2} \mathbf{r}_{(i,j)}$. This requires defining the double sum
 over rotation matrices $\bar{\bar{\mathbf{S}}}(n) = \sum_{n'=0}^{n-1} \bar{\mathbf{S}}(n')$. These matrices will take the same form as Eqn. 8 with its components replaced by
 $\bar{\bar{\cos}}(n\theta)$, $\bar{\bar{\sin}}(n\theta)$, and $n(n-1)/2$. The double-sums over the trigonometric functions require no additional evaluation when we
 rewrite $\cos(\frac{\theta}{2} - n\theta) = \cos(\frac{\theta}{2}) \cos(n\theta) + \sin(\frac{\theta}{2}) \sin(n\theta)$ in $\bar{\bar{\sin}}(n\theta)$ since we can simply substitute our previous results to find

$$\begin{aligned} \bar{\bar{\cos}}(n\theta) &= \frac{1}{2} \left(n - \bar{\bar{\cos}}(n\theta) + \cos(\frac{\theta}{2}) \bar{\bar{\sin}}(n\theta) \right), \\ \bar{\bar{\sin}}(n\theta) &= \frac{1}{2} \left(n \cos(\frac{\theta}{2}) - \cos(\frac{\theta}{2}) \bar{\bar{\cos}}(n\theta) - \sin(\frac{\theta}{2}) \bar{\bar{\sin}}(n\theta) \right) \csc(\frac{\theta}{2}). \end{aligned} \quad [28]$$

The vertex displacements can then be written in the similar form

$$\begin{aligned} \mathbf{u}_k(\mathbf{n}) &= \bar{\mathbf{S}}_1(n_1) \sum_{(i',j',k')}^{n_1=1} (\boldsymbol{\omega}_{(i',j',k')} \times \mathbf{r}_{(i',k')}) + \mathbf{S}_1^{n_1} \bar{\mathbf{S}}_2(n_2) \sum_{(i',j',k')}^{n_2=1} (\boldsymbol{\omega}_{(i',j',k')} \times \mathbf{r}_{(i',k')}) \\ &+ \bar{\bar{\mathbf{S}}}_1(n_1) (\mathbf{\Omega}_1 \times \mathbf{l}_1) + \mathbf{S}_1^{n_1} \bar{\bar{\mathbf{S}}}_2(n_2) (\mathbf{\Omega}_2 \times \mathbf{l}_2) + (\bar{\mathbf{S}}_1(n_1) \mathbf{\Omega}_1) \times (\mathbf{S}_1^{n_1} \bar{\mathbf{S}}_2(n_2) \mathbf{l}_2). \end{aligned} \quad [29]$$

139 Again, the first two terms have the interpretation of intracell strains and the last three terms signify changes in intercell
 140 curvatures.

141 We can similarly compute changes in the lattice rotation axes after a linear folding motion. The new axis must be invariant
 142 under the new rotation

$$\mathbf{S}' \hat{s}' = (\mathbf{I} + \delta\mathbf{S}) \mathbf{S} (\hat{s} + \delta\hat{s}) = \hat{s}', \quad [30]$$

144 where for the moment we drop the subscripts indicating which lattice direction these rotations are in. To first-order, this gives

$$(\mathbf{I} - \mathbf{S}) \delta\hat{s} = \delta\mathbf{S} \hat{s}. \quad [31]$$

146 Since $\delta\hat{s}$ must be orthogonal to \hat{s} , we can project into the plane defined by \hat{s} as we did for position compatibility, Eqn. 4

$$(\mathbf{I} - \mathbf{S}^\perp) \delta\hat{s}^\perp = (\delta\mathbf{S} \hat{s})^\perp. \quad [32]$$

148 By the independence of summation order in

$$\boldsymbol{\omega}_{(i,j,k)}(\mathbf{n}) = \sum_{(i',j')} \phi_{(i',j')}(\mathbf{n}') \hat{r}_{(i',j')}(\mathbf{n}'), \quad [33]$$

150 the cell angular velocities obey a similar relation to Eqn. 5 for the lattice vectors

$$\mathbf{\Omega}_2^\perp = (\mathbf{I} - \mathbf{S}_1^\perp)^{-1} (\mathbf{I} - \mathbf{S}_2^\perp) \mathbf{\Omega}_1^\perp, \quad [34]$$

152 so that after inversion

$$\delta\hat{s}_{1,2}^\perp = (\mathbf{I} - \mathbf{S}_{1,2}^\perp)^{-1} (\mathbf{\Omega}_{1,2} \times \hat{s})^\perp, \quad [35]$$

154 we have $\delta\hat{s}_1^\perp = \delta\hat{s}_2^\perp$.

155 8. Origami reconstruction

156 Here, we show how to reconstruct an origami sheet from its fold angles. Starting with edge $\hat{r}_{(1,2)} \equiv \hat{x}$, we can obtain
 157 $\hat{r}_{(1,3)} = \mathbf{R}_z(\alpha_{(1,2,3)}) \hat{r}_{(1,2)}$ by choosing the normal of this first face to lie in the xy plane. We may similarly obtain successive
 158 edges, however the normal vectors of successive faces are not known. Instead, we use the fact the rotation about some axis, \hat{z}' ,
 159 is given $\mathbf{R}_{z'}(\alpha) = \mathbf{R}_x(\rho) \mathbf{R}_z(\alpha) \mathbf{R}_x^{-1}(\rho)$ when \hat{z}' is related to \hat{z} by a rotation of ρ about \hat{x} . Since we know the fold angles which
 160 relate the normal vectors on successive faces in addition to the direction of the previous edge vector, we are able to use this
 161 method to find the direction for each edge leaving a vertex. Moreover, since the edge lengths are preserved by a rigid folding
 162 motion, once we have the directions of the edges we can find the positions of the connected vertices. By this method, we can
 163 determine the positions of all vertices in the unit cell, as well as those which are connected to a vertex in the unit cell by a
 164 crease.

165 This latter fact implies we obtain information about how edges rotate between cells which we use to determine the lattice
 166 rotations. To be specific, given two edges in the unit cell and their counterpart in either the cell (1, 0) or (0, 1), we can construct
 167 an orthonormal basis for a plane in either cell and define the invertible matrix

$$\mathbf{B} = \left[\hat{r}_{(i,j)} \quad \hat{r}'_{(k,l)} \quad \widehat{\mathbf{r}_{(i,j)} \times \mathbf{r}'_{(k,l)}} \right]^T \quad [36]$$

169 where we have used Gram-Schmidt orthogonalization so that $\hat{r}'_{(k,l)} \cdot \hat{r}_{(i,j)} = 0$. The matrix in an adjacent cell must be related
 170 $\mathbf{B}_{1,2} = \mathbf{S}_{1,2}\mathbf{B}$ so that the cell rotations can be written explicitly as $\mathbf{S}_{1,2} = \mathbf{B}_{1,2}\mathbf{B}^{-1}$. The coresponding rotation angle is then
 171 given by $\theta_{1,2} = \arccos(\text{Tr}\mathbf{S}_{1,2} - 1)/2$ and the rotation axis is given by introducing a normalization factor, N , to the vector

$$172 \quad \hat{s} = \frac{N}{2 \sin \theta} (S_{1,2}^{32} - S_{1,2}^{23}, S_{1,2}^{13} - S_{1,2}^{31}, S_{1,2}^{12} - S_{1,2}^{21}), \quad [37]$$

173 where we use superscripts to denote components of the rotation matrix. The lattice vectors in the unit cell are more simply
 174 computed by summing along the edges which connect the first vertex to its counterpart in the neighboring cells. Once we
 175 have the positions for all vertices in the unit cell, the lattice vectors, and the lattice rotations we can reconstruct our periodic,
 176 cylindrical sheet. By doing this along the trajectory, we are able to show the origami sheet rigidly folding in real time.

177 9. Projection into strain space

178 Here, we explain the orthonormalization used for our deformation tensor. To construct the components of the deformation
 179 tensor used to visualize the configuration space of our rigidly foldable origami sheet we introduce the first fundamental
 180 form, $\tilde{g}_{(i,j)} = \mathbf{l}_i \cdot \mathbf{l}_j$, of the unit cell. This quantity can be used to compute distances in reference to the initially flat sheet
 181 $ds^2 = \tilde{g}_{(i,j)} \Delta n_i \Delta n_j$, where Δn_i is the integer number of cells translated in the i lattice direction. Changes to this quantity
 182 give a description of the stretching and shearing of the lattice vectors as the sheet evolves. For consistency, we perform a
 183 coordinate transformation so that the first fundamental form of the flat state is the identity matrix. We write this new quantity
 184 $g_{ij} = a_{ik}^{-1} \tilde{g}_{kl} a_{lj}^{-1}$, where $a_{ij} = \hat{e}_i \cdot \mathbf{l}_j$ for the unit vectors \hat{e}_i lying within the plane of the flat sheet. We can then construct the
 185 deformation tensor, $\epsilon = \mathbf{g} - \mathbf{I}$, whose three independent components, $(\epsilon_{11}, \epsilon_{22}, \epsilon_{12})$, provide a three-dimensional coordinate
 186 system to visualize the path of our origami sheet through its configuration space.

187 10. Periodic and boundary modes

188 In this Appendix we briefly describe the periodic and boundary modes of mechanical frames in general and the triangulated
 189 origami sheets discussed in the main text in particular, as well as their relations to quantum systems.

190 This article concerns itself with characterizing the isometries of triangulated origami sheets. Because a triangular frame is
 191 rigid, each of those isometries corresponds exactly to a set of vertex positions that do not stretch any of the sides of any of
 192 the triangular faces. Consequently, we can identify the linear zero modes of our triangulated origami surface by identifying
 193 the linear zero modes of a ‘‘ball and spring’’ structure with vertices located at origami vertices and inextensible bonds along
 194 origami edges.

195 We may then construct a linear map from vertex displacements $\mathbf{u}_1, \mathbf{u}_2$ to the extension of the bond between them as

$$e = (\mathbf{u}_2 - \mathbf{u}_1) \cdot \hat{r}_{12}, \quad [38]$$

196 where \hat{r}_{12} is the unit vector pointing from the first to the second vertex. In a periodic system such as the ones we consider here,
 197 Bloch’s theorem would generally indicate that the only waveforms which could be normal modes of the system (that is, modes
 198 that oscillate at some frequency, importantly including zero modes that oscillate at zero frequency) would be those modes that
 199 scaled by phase factors between neighboring cells. In fact, before periodic boundary conditions are imposed, this ‘‘phase factor’’
 200 need not have unit magnitude and so to represent a generalized Bloch mode we define two complex numbers, z_1, z_2 by which a
 201 potential normal mode may scale between the two origami lattice directions. In terms of these, we may define the rigidity map
 202 $\mathbf{R}(z_1, z_2)$ from a vector \mathbf{u} describing the displacements of all the sites in the unit cell to a vector \mathbf{e} describing the extensions of
 203 all the bonds (origami edges) in the unit cell:

$$\mathbf{e} = \mathbf{R}(z_1, z_2)\mathbf{u}. \quad [39]$$

204 Because our systems are both triangulated and periodic, this rigidity map is a square matrix. This can be seen via Euler’s
 205 theorem for a polyhedron, $V + F - E = \chi$. In this case, the Euler characteristic χ vanishes, because the periodic boundary
 206 conditions give our unit cell the surface topology of a torus. Furthermore, because triangles have three edges but each edge is
 207 shared between two triangles, $E = (3/2)F$. Thus, throughout the entire unit cell there are three edges for each vertex, even if
 208 not all vertices are adjacent to six edges. Since origami vertices can be displaced in three directions while edge extensions are
 209 scalars, this ensures that the rigidity map is a square matrix. Because the matrix is square but not generally Hermitian, it can
 210 be interpreted as the Hamiltonian of a dissipative quantum system. Further, this square matrix implies zero modes exist for
 211 generalized phase factors z_1, z_2 if and only if its determinant vanishes:

$$\det(\mathbf{R}(z_1, z_2)) = 0. \quad [40]$$

212 To that end, when one of the complex numbers is held fixed, locating the zero modes amounts to finding zeros of some
 213 function $f(z)$ in the complex plane. Because of the Argument Principle of complex analysis, one may calculate the number of
 214 zero modes with $|z| < 1$ by calculating the change in phase of $f(z)$ as one winds around the unit circle $|z| = 1$. Physically, this

215 establishes a bulk-boundary correspondence between the number of zero modes exponentially localized to one edge and the
 216 winding of the bulk modes, the Kane Lubensky topological invariant.

217 Although Newtonian dynamics is second-order in time, Kane and Lubensky compose the vertex displacements and edge
 218 extensions into a combined vector space governed by first-order dynamics. This thus assumes the form of a Schrödinger
 219 equation, with a Hamiltonian containing both the rigidity and equilibrium matrices, lying in the BDI symmetry class.

220 Generically, this can lead to excesses or deficits of zero modes in such mechanical systems. However, it has been previously
 221 observed that no such excesses seem to occur in triangulated origami. We prove this via consideration of the *states of self stress*.

222 Just as the extensions of bonds were determined in terms of the displacements of adjoining vertices above, we may also
 223 write the total force on a vertex in terms of the sum of the tensions t_α and the edge orientations \hat{r}_α :

$$\mathbf{f} = \sum_{\alpha} t_{\alpha} \hat{r}_{\alpha}. \quad [41]$$

224 Consequently, if we assume unit-stiffness springs, such that tensions are extensions we can construct a map from the bond
 225 extensions in a unit cell to the forces on the sites as

$$\mathbf{f} = \mathbf{R}^T(1/z_1, 1/z_2)\mathbf{e}. \quad [42]$$

226 Here the linear map, known as the equilibrium map, is the transpose of the rigidity map, evaluated as the inverses of the
 227 complex numbers, or at the opposite (complex) wavevector. States of self stress are defined as the vectors in the nullspace of
 228 this map, sets of tensions (stresses) that do not support an external stress. The reason for the inversion of the complex numbers
 229 that if a mode rescales by a factor z_1 as one translates one cell to the right then if a site in one cell connects to a bond in the
 230 cell to the right, the bond extensions has a factor of z relative to the site displacement/force, but the site displacement/force
 231 has a factor of $1/z$ relative to the bond extension.

232 From the rank-nullity theorem of linear algebra, we then find that the number of zero modes at a complex wavevector is
 233 equal to the number of states of self stress at the opposite wavevector.

234 However, origami has a special feature not common to generic mechanical systems. The full nonlinear Belcastro Hull can be
 235 linearized into the same form as the self stress condition (see Appendix 4 and main text). At any finite wavevector, these
 236 dihedral angle changes can be integrated to obtain vertex displacements at the same wavevector. The process also works in
 237 reverse, and hence in a triangulated origami system there is exactly one zero mode at any complex wavevector for each state of
 238 self stress at the *same* wavevector.

239 Combining the results of the two previous paragraphs, we then find that in triangulated origami there must be equal
 240 numbers of zero modes present on opposite edges, ensuring that the system never becomes topologically polarized in the Kane
 241 Lubensky sense.

242 However, this does not render origami sheets topologically trivial. In fact, they possess a \mathbb{Z}_2 topological invariant, in contrast
 243 with the integer invariant of Kane Lubensky polarization. This invariant represents an intriguing possibility for realizing new
 244 protected modes at surfaces and interfaces. In the absence of this hidden origami duality between zero modes and states of self
 245 stress, such an interface mode would be possible only by enforcing some spatial symmetry, as well as critical coordination.

246 Finally, we note that because zero modes appear at opposite complex wavevectors, the determinant of the rigidity matrix
 247 must appear as a symmetrical Laurent polynomial, as discussed in the main text. This means that the rigidity matrix is
 248 real in the Brillouin Zone. Consequently, it can be positive or negative and generically the regions of the BZ in which it
 249 shifts from positive to negative are curved one-dimensional lines hosting finite-wavevector bulk zero modes. This feature is in
 250 contrast with generic critically coordinated mechanical frames, which instead host Weyl points at zero-dimensional points in a
 251 two-dimensional BZ.

252 These lines have also been predicted in quantum spin systems. In kagome lattices with spins of variable orientations but
 253 fixed coupling strengths, energetic contributions can be minimized when the weighted sums of spin orientations on a single
 254 kagome triangle vanish. Hence, the ground state of such a system corresponds to orientations of fixed length edges in which
 255 trios of vectors sum to zero. These in fact correspond exactly to isometries of triangulated origami sheets, as described in the
 256 references in the main text. In the latter case, the vectors summing to zero while remaining of fixed length ensures that each
 257 triangular face remains intact and undeformed. Consequently, the zero-energy magnetic excitations of the quantum system
 258 (magnons) mirror the zero-energy deformations of the classical origami.

259 In summary, the spatially varying zero modes of triangulated origami exist as a special class within the broader zero
 260 modes of mechanical frames, with strikingly non-generic features protected not by spatial symmetries but by the nature of the
 261 triangulated origami as both critically coordinated and an intact surface with a guaranteed duality.

262 **Movie S1. Nondevelopable origami rigid folding animation.**

263 **Movie S2. Developable origami rigid folding animation.**